NASA Technical Memorandum 81506

FAR-FIELD RADIATION OF AFT TURBOFAN NOISE

Edward J. Rice and Arthur V. Saule
Lewis Research Center
Cleveland, Ohio

Prepared for the
Ninety-ninth Meeting of the
Acoustical Society of America
Atlanta, Georgia, April 21-25, 1980

FAR-FIELD RADIATION OF AFT TURBOFAN NOISE

by Edward J. Rice and Arthur V. Saule

National Aeronautics and Space Administration
Lewis Research Center
Cleveland, Ohio 44135

ABSTRACT

The far-field radiation of turbofan noise from the inlet of an engine has recently received considerable study. Relatively simple approximate expressions have been developed for single mode radiation as a function of cut-off ratio and for multimodal radiation. Convective effects upon radiation which are essential for interpreting static engine tests have been determined. This information is essential for the design of inlet suppressors. This paper represents an initial effort to provide similar approximate expressions for the noise radiation from the aft duct. The results of approximate aft radiation equations compare favorably to more exact Wiener-Hopf radiation results. Refraction as well as convective effects in the multiple flow streams must be considered. The peak in the radiation pattern, which occurs nearly at engine sideline, is composed of modes with relatively large cut-off ratios. This implies that aft fan radiation will be inherently more difficult to suppress than the fan inlet noise. The theoretical multimodal radiation pattern is compared to experimental data for the first two harmonics of blade passage frequency for three full scale fans at two speeds. The agreement between theory and experiment is quite good.

E-444

INTRODUCTION

Far-field radiation theory for sound radiation from engine ducts is essential to noise suppressor studies. First, it is required to translate the sound attenuation occurring in the duct to the more useful information of sound attenuation in the far-field[1,2] of the engine. Second, the radiation theory, when compared to noise directivity data, can be used to infer information about either the modal power distribution[3,4,5] or the acoustic power distribution versus mode cut-off ratio[6,7] which exists in the engine duct.

Sound radiation from the inlet duct has been studied extensively. Tyler and Sofrin[8] developed a flanged duct radiation model which was shown to provide a reasonable representation to experimental data. Lansing, et al.[9] and Homicz and Lordi[10] developed Wiener-Hopf radiation solutions for an unflanged duct. Cho[11] presented sound radiation solutions for hyperboloidal inlet ducts which were favorably compared to experimental data by Clark and Cho.[12] There are serious limitations on all of these exact analytical solutions as presented. The flanged duct and hyperboloidal inlet solutions are currently formulated only for zero steady flow both in the duct and in the surrounding environment. The Wiener-Hopf solutions can accomodate steady flow but only for the same flow velocity in the duct and in the surrounding region, or else for a tube of high velocity flow separated from the ambient flow by a slip layer. Neither of these flow situations are realistic for real engine inlets, especially at static test conditions. Under static test, the flow velocity is very high in the duct while outside there is essentially zero flow at all angles from the

inlet axis. This more realistic but complicated flow situation was analyzed approximately by Rice, et al.[4] For the two cases, no flow and equal flow everywhere, which can be handled by the Wiener-Hopf method, the far-field radiation angle for the peak of the principal lobe of radiation was found to be coincident with the angle of propagation with respect to the axis for the mode in the inlet duct. This observation led to using simple angle transformations to account for the local effect of flow on the principal lobe of radiation in going from the high Mach number in the duct to a different flow Mach number in the ambient medium. This method was indirectly confirmed by its ability to explain far-field directivity attenuation patterns[1,2] and more directly, by observation of single mode direcitivity patterns in a static engine test.[5] Heidmann, et al.[5] also generalized the above approximate theory by extending the duct flow transformation to include any angle instead of only the angle of the principal lobe of radiation considered in reference 4.

Some other observations concerning the far-field radiation theories should be made. Lansing, et al.[9] have shown that except in the vicinity of the duct flange, the flanged and unflanged duct radiation solutions are almost identical. Homicz and Lordi[10] have amplified this correspondence by deriving the zeroes (cancellations) in the unflanged duct Wiener-Hopf solutions and they are seen to coincide with those of the flanged duct solutions. Flanged duct radiation solutions are much simpler in form and use than the Wiener-Hopf solutions, which require complex computer programs for evaluation. The simpler closed form solutions should always be used when they are sufficiently accurate. They also yield to approximations which allow the direct derivation of simple expressions for multimodal radiation patterns. These multimodal radiation patterns have been presented by Rice[6] for zero steady flow and have been found to adequately reproduce exact radiation calculations.[6,7] These simple expressions have been found useful in inferring the distribution of acoustic power versus mode cut-off ratio for sound with randomly generated modes, such as broad-band noise or even tones found in static engine tests.[6]

The far-field radiation theory for the aft duct case has received much less attention than that for the inlet. This may be due to the complex multiple flow streams at several Mach numbers which make up a typical exhaust duct system. However, compared to the inlet case, the Wiener-Hopf solution should provide a more realistic modelling of sound propagation through the exhaust flow streams with slip layers. Wiener-Hopf radiation solutions have been presented by Savkar and Edelfelt[13] and Savkar[14] for a single jet stream with a flow mismatch with the ambient environment. These exact solutions are used as a base for checking simpler approximate solutions.

The purpose for the work reported in this paper is thus to generate approximate radiation expressions for the aft duct, in the same spirit as was done for the inlet, and check these simple expressions against the available exact solutions. The starting point for this approximate analysis is the known propagation angle for a mode in the exhaust duct with flow. An angle transformation is performed to obtain the direction of the vector normal to the wavefront. Refraction is then considered through the slip layer and, finally, another angle transformation is required if there is an ambient flow velocity. Also, the flanged duct radiation equation is cast in a form which is usable for the aft duct. The above transformations are required to generate the far-field radiation pattern. The simplified radiation patterns are then compared to the exact single mode solutions. A simple multimodal radiation pattern is then generated from the approximate expressions. Results from this simple equation and data from three full scale fans at two frequencies and speeds are compared to a laboriously obtained exact multimodal radiation pattern.

The approximate expressions obtained here are essential for the development of an aft duct liner design and evaluation program analogous to the inlet program reported in reference 1.

SYMBOLS

c	speed of sound, m/sec
c_D	c in exhaust duct and jet, m/sec
c_f	c in far-field surrounding medium, m/sec
D	duct diameter, m
f	frequency, Hz
i	far-field angle index in equation (38)
J'_m	derivative of Bessel function of first kind of order m with respect to its argument
M_D	Mach number in exhaust duct and jet
M_f	Mach number in surrounding medium
m	spinning mode lobe number
N	relative number of modes, see equations (34) and (35)
P	acoustic pressure, N/m^2
P_i	acoustic pressure at i^{th} far-field angle, N/m^2
P_{fM}	multimodal P in far-field with duct flow, see equation (36), N/m^2
P_{fP}	principal lobe peak P in far-field with duct flow, see equation (31), N/m^2
P_P	principal lobe peak P, flanged duct, no flow, see equation (22), N/m^2
R	radius from duct exit to far-field observation point, m
ΔS_0	far-field area subtended by principal lobe, no flow, see equations (26) and (29), m^2
ΔS_f	far-field area subtended by principal lobe, with duct flow, see equation (30), m^2
SPL_f	multimodal sound pressure level in far-field with duct flow
W	acoustic power, Nm/sec
$\alpha_{m\mu}$	hardwall eigenvalue for (m, μ) mode
β	$\sqrt{1 - M_D^2}$
η	frequency parameter, fD/c
$\overline{\eta}$	frequency parameter transformed to steady flow, η/β
μ, ν	radial mode index, $\mu = 1$ is lowest order
ξ_D	mode cut-off ratio with duct flow, see equation (8)
ξ_{D1}	see equation (32)

ξ_{D2} see equation (33)

ξ_0 mode cut-off ratio, no flow

ρ density, kg/m^3

φ angle between phase velocity vector and duct axis, deg

φ_D φ in duct with flow, deg

φ_f φ in far-field, deg

ψ angle between group velocity vector and duct axis, deg

$\bar{\psi}$ group velocity angle transformation to introduce steady flow, see equation (5), deg

ψ_D ψ in duct with flow, deg

ψ_f ψ in far-field with duct flow, deg

ψ_{fP} ψ_f at principal lobe peak, deg

ψ_{fZ} ψ_f at zeroes of radiation pattern, deg

ψ_{fZS} ψ_f at boundary of zone of silence, deg

ψ_0 ψ in far-field, no flow, deg

ψ_{0P} ψ_0 at principal lobe peak, deg

ψ_{01} ψ_0 at zero of principal lobe below peak, deg

ψ_{02} ψ_0 at zero of principal lobe above peak, deg

APPROXIMATE RADIATION THEORY

In this section the flanged duct radiation equations which are to be used are presented. The several angle transformations required are also given. The geometry considered is a circular jet with a flow Mach number M_D discharging into a surrounding medium with Mach number M_f (symbols are defined in the Symbol List). The subscript D refers to the duct and its related jet while subscript f refers to the far-field or surrounding medium. The angles φ are between the duct axis and the phase velocity vector (normal to the wave front) while angles ψ are between the duct axis and the group velocity vector. For zero flow φ and ψ are the same. Although the transformation are derived for the general condition, the surrounding medium will be assumed at rest as in a static engine test for the results discussed in this paper.

Radiation Equations and Angle Transformations

The far-field mean-squared pressure radiation expression for a flanged circular duct for equal acoustic power per mode[3,6] and zero flow can be expressed as,

$$p^2 = \frac{\sqrt{1 - \left(\frac{\alpha_{m\mu}}{\pi\eta}\right)^2}\ \sin^2\psi_0 [J'_m(\pi\eta \sin \psi_0)]^2}{\left[1 - \left(\frac{m}{\alpha_{m\mu}}\right)^2\right]\left[\left(\frac{\alpha_{m\mu}}{\pi\eta}\right)^2 - \sin^2\psi_0\right]^2} \qquad (1)$$

where the subscript on ψ_0 denotes zero velocity and the frequency parameter is

$$\eta = \frac{fD}{c} \tag{2}$$

and the mode eigenvalue $\alpha_{m\mu}$ is determine from

$$J'_m(\alpha_{m\mu}) = 0 \tag{3}$$

An approximate version of equation (1) has been reported[6] using the sine approximation for the Bessel function and requiring $(m/\alpha_{m\mu})^2 \ll 1$. This expression, which will be useful in a later discussion, is,

$$p^2 \propto \frac{2 \sin \psi_0 \sqrt{1 - \left(\frac{\alpha_{m\mu}}{\pi\eta}\right)^2} \left\{\sin\left[\pi\eta\left(\sin \psi_0 - \frac{\alpha_{m\mu}}{\pi\eta}\right)\right]\right\}^2}{\pi^2\eta\left[\left(\frac{\alpha_{m\mu}}{\pi\eta}\right)^2 - \sin^2\psi_0\right]^2} \tag{4}$$

The first transformation required is to introduce uniform flow into equation (1) by using a coordinate stretching technique.[9,10,15] It may seem physically strange to have uniform steady flow with a flanged duct configuration, but the final results will justify its use. The transformation involves replacing ψ_0 by $\overline{\psi}$ such that

$$\sin \overline{\psi} = \frac{\beta \sin \psi_D}{\sqrt{1 - M_D^2 \sin^2\psi_D}} \tag{5}$$

and replacing η by

$$\overline{\eta} = \frac{\eta}{\beta} \tag{6}$$

where

$$\beta = \sqrt{1 - M_D^2} \tag{7}$$

In addition the mode cut-off ratio with flow is,

$$\xi_D = \frac{\pi\eta}{\alpha_{m\mu}\sqrt{1 - M_D^2}} = \frac{\pi\eta}{\alpha_{m\mu}\beta} \tag{8}$$

When equations (5) to (8) are used in equation (1) the result is,

$$p^2 = \frac{\beta^2 \sqrt{1 - \frac{1}{\xi_D^2}} \sin^2\psi_D \left[J'_m \left(\frac{\pi\eta \sin\psi_D}{\sqrt{1 - M_D^2 \sin^2\psi_D}} \right) \right]^2}{\left[1 - \left(\frac{m}{\alpha_{m\mu}} \right)^2 \right] \left[1 - M_D^2 \sin^2\psi_D \right] \left[\frac{1}{\xi_D^2} - \frac{\beta^2 \sin^2\psi_D}{\left(1 - M_D^2 \sin^2\psi_D \right)} \right]^2} \tag{9}$$

Equation (9) describes the radiation in a uniform flow field and should adequately reproduce the results for an unflanged duct, except in the vicinity of the flange where some error will occur. With the Mach number M_D in the radiation expression, there are more propagating modes than with $M_D = 0$. This can be seen from equation (8), where for a given frequency parameter (η) and duct mode (eigenvalue $\alpha_{m\mu}$) the cut-off ratio is higher with uniform flow. Cut-off occurs when $\xi_D = 1$.

The second transformation yields the phase velocity vector propagation angle φ_D, which is required for the refraction expression through the flow discontinuity at the jet boundary. Figure 1 shows the several angles involved. The angle φ_D is related to the group velocity vector angle ψ_D by,

$$\cos\psi_D = \frac{M_D + \cos\varphi_D}{\sqrt{1 + M_D^2 + 2M_D \cos\varphi_D}} \tag{10}$$

as discussed in reference 4. Equation (10) is then inverted to yield,

$$\cos\varphi_D = -M_D \sin^2\psi_D + \sqrt{M_D^2 \sin^4\psi_D - \left(1 + M_D^2\right)\sin^2\psi_D + 1}$$

$$= -M_D \sin^2\psi_D + \cos\psi_D \sqrt{1 - M_D^2 \sin^2\psi_D} \tag{11}$$

The refraction through the slip layer between the aft duct jet and the surrounding medium can now be calculated. This is done in the simplest way by considering the refraction of an oblique plane wave upon a plane slip layer, as can be found in reference 16. The propagation angle of the phase velocity emerging from the slip layer into the surrounding medium is,

$$\cos\varphi_f = \frac{c_f \cos\varphi_D}{c_D + (c_D M_D - c_f M_f)\cos\varphi_D} \tag{12}$$

Finally, the direction of the group velocity vector in the far-field can be derived in a manner parallel to that of equation (10) to obtain,

$$\cos\psi_f = \frac{M_f + \cos\varphi_f}{\sqrt{1 + M_f^2 + 2M_f \cos\varphi_f}} \tag{13}$$

The angle ψ_f is the far-field radiation angle used for plotting the transformed flanged duct radiation pattern.

The simpler case will be considered in all that follows, in which the surrounding medium is static ($M_f = 0$) and both media have the same temperature so that $c_f = c_D = c$. Equations (12) and (13) then simplify to,

$$\cos \varphi_f = \frac{\cos \varphi_D}{1 + M_D \cos \varphi_D} \tag{14}$$

and

$$\cos \psi_f = \cos \varphi_f \tag{15}$$

The angle transformations from equations (11), (14), and (15) can be combined to yield,

$$\cos \psi_f = \frac{-M_D \sin^2\psi_D + \sqrt{M_D^2 \sin^4\psi_D - \left(1 + M_D^2\right)\sin^2\psi_D + 1}}{1 - M_D^2 \sin^2\psi_D + M_D \sqrt{M_D^2 \sin^4\psi_D - \left(1 + M_D^2\right)\sin^2\psi_D + 1}}$$

$$= \frac{-M_D \sin^2\psi_D + \cos \psi_D \sqrt{1 - M_D^2 \sin^2\psi_D}}{1 - M_D^2 \sin^2\psi_D + M_D \cos \psi_D \sqrt{1 - M_D^2 \sin^2\psi_D}} \tag{16}$$

Values of ψ_D can now be inserted into equation (9) to calculate p^2 from which the sound pressure level can be calculated, and finally the radiation angle in the far-field can be calculated from equation (16).

Comparison of Approximate and Exact Single Mode Radiation Theory

The approximate radiation expressions as presented in the previous section were exercised for the (8, 4) mode (i.e., $m = 8$, $\mu = 4$). This mode was chosen because it has several sidelobes on each side of the principal lobe. The convention used here is that the lowest radial mode has $\mu = 1$. The exact Wiener-Hopf solution[13] was generated using a program available in the NASA-Langley computer. Both solutions are plotted in figure 2. The agreement between the two curves is very good. Most important is the fact that the principal lobe location and shape are very accurately reproduced. The zeroes or nodes are also accurately located. Some error occurs in the amplitude of the side lobes. The accuracy of the approximate method is all the more surprising since there are several other physical phenomena (included in the exact solution) which could be added to the theory but have not been completed at this time. Internal reflection at the slip layer as a function of propagation angle should be included. The various angles involved in the flanged duct solution are shifted differently by the refraction at the slip layer. This involves far-field area changes which should be accounted for (some discussion occurs in a later section) to retain acoustic power equality. Also it is known that at the flange, the flanged duct solution yields results which are

high compared to the unflanged duct solution, due to reflection off the flange. This could be corrected approximately.

Location of the Principal Lobe and the Zeroes

The critical values of the approximate far-field radiation theory will occur when the argument of the derivative of the Bessel function in equation (9) is equal to a duct eigenvalue, i.e.,

$$\frac{\pi\eta \sin \psi_D}{\sqrt{1 - M_D^2 \sin^2\psi_D}} = \alpha_{m\nu} \tag{17}$$

If the (m, μ) mode is considered, then the location of the peak of the principal lobe will be found when $\nu = \mu$. Note the denominator of equation (9) also vanishes at this point and a finite limit is found for the amplitude. When $\nu \neq \mu$ only the numerator of equation (9) vanishes and the several zeroes are located. By using the transformations given by equations (11), (14), and (15), equation (17) can be reduced to,

$$\cos \psi_{fP} = \frac{-M_D + \left(\frac{\pi\eta}{\alpha_{m\mu}}\right)\sqrt{\left(\frac{\pi\eta}{\alpha_{m\mu}}\right)^2 - \beta^2}}{\left(\frac{\pi\eta}{\alpha_{m\mu}}\right)\left[\frac{\pi\eta}{\alpha_{m\mu}} + M_D\sqrt{\left(\frac{\pi\eta}{\alpha_{m\mu}}\right)^2 - \beta^2}\right]} \tag{18}$$

which gives the principal lobe peak location and,

$$\cos \psi_{fZ} = \frac{-M_D + \left(\frac{\pi\eta}{\alpha_{m\nu}}\right)\sqrt{\left(\frac{\pi\eta}{\alpha_{m\nu}}\right)^2 - \beta^2}}{\left(\frac{\pi\eta}{\alpha_{m\nu}}\right)\left[\frac{\pi\eta}{\alpha_{m\nu}} + M_D\sqrt{\left(\frac{\pi\eta}{\alpha_{m\nu}}\right)^2 - \beta^2}\right]} \tag{19}$$

which gives the zeroes for the (m, μ) mode. Note that the mode cut-off ratio (ξ_D) for the (m, μ) mode can be introduced into equation (18) to yield,

$$\cos \psi_{fP} = \frac{-M_D + \beta^2\xi_D\sqrt{\xi_D^2 - 1}}{\beta^2\xi_D\left(\xi_D + M_D\sqrt{\xi_D^2 - 1}\right)} \tag{20}$$

Note that the location of the principal lobe is a function only of the mode cut-off ratio and the Mach number. All modes with similar cut-off ratios will radiate similarly to the far-field just as in the zero Mach number case.[6]

The results of equations (18) and (19) are compared to exact Wiener-Hopf solutions in figure 3 for four modes. The approximate principal lobe peak and

the zeroes are denoted by arrows. Note that the agreement is excellent. Some derivation has been noted in other plots (not shown) when the principal lobe is located far ahead of the sideline ($\psi_f > 90^o$). It is not known whether the approximate theory or the exact theory has deficiencies in this range.

It should be noted that the equations in this section were derived for a static surrounding medium. For $M_f \neq 0$, equations (12) and (13) should be used in the derivation instead of equations (14) and (15).

Zone of Relative Silence

If $\psi_D = 0$ is used in equation (16) the limiting angle for the zone of silence can be defined as,

$$\cos \psi_{fZS} = \frac{1}{1 + M_D} \tag{21}$$

For the example radiation patterns shown so far in this paper with $M_D = 0.6$, the boundary of the zone of silence is at $\psi_f = 51.32^o$. Thus, in the approximate theory used here, there is no radiation at all predicted between the aft duct axis and $\psi_f = 51.32^o$. This result is of course the consequence of the simple refraction model (equations (12) or (14)) used across the slip layer. The exact Wiener-Hopf technique also shows an abrupt change at $\psi_f = 51.3^o$ as shown in figures 2 and 3. However, these exact solutions show some radiation within the zone of silence although the levels are very low.

Multimodal Far-Field Radiation Model

In this section, the approximate multimodal radiation equation developed in reference 6 will be extended to include the duct jet flow and the refraction through the slip layer. This simple approximate equation will then be compared to the exact multimodal Wiener-Hopf solution, which is quite cumbersome to generate. Equal acoustic power per mode will be considered here, but the development could be easily generalized by using a cut-off ratio biasing function.[6,7]

Approximate theory. - The technique used here will be illustrated by expanding upon the zero Mach number theory developed in reference 6. The approximate single mode radiation equation (4) will be used as a starting point since it is quite a good approximation to equation (1) but is much easier to use. At the peak of the principal lobe in the far-field, equation (4) yields,[6]

$$P_P^2 \approx \frac{\eta \xi_0 \sqrt{1 - \frac{1}{\xi_0^2}}}{2} = \frac{\eta \cos \psi_{OP}}{2 \sin \psi_{OP}} \tag{22}$$

where the zero Mach number cut-off ratio is obtained from equation (8) with $M_D = 0$ and the principal lobe location is given by,[6]

$$\sin \psi_{OP} \approx \frac{1}{\xi_0} \tag{23}$$

From equation (4) it can be seen that the zeroes in P^2 extend around the principal lobe peak at angles

$$\sin \psi_{01} \approx \frac{1}{\xi_0} - \frac{1}{\eta} \approx \sin \psi_{0P} - \frac{1}{\eta} \tag{24}$$

$$\sin \psi_{02} \approx \frac{1}{\xi_0} + \frac{1}{\eta} \approx \sin \psi_{0P} + \frac{1}{\eta} \tag{25}$$

The far-field incremental area subtended by the principal lobe can thus be estimated by,

$$\Delta S_0 = 2\pi R^2 \int_{\psi_{01}}^{\psi_{02}} \sin \psi_0 \, d\psi_0 \approx 2\pi R^2 \sin \psi_{0P} (\psi_{02} - \psi_{01}) \tag{26}$$

where a small angle increment is assumed. A first order expansion of ψ_{01} and ψ_{02} around ψ_{0P} can be made assuming $1/\eta$ is very small so that $\psi_{02} - \psi_{01}$ can be estimated as,

$$\psi_{02} - \psi_{01} \approx \frac{2}{\eta \cos \psi_{0P}} \tag{27}$$

Using equation (27) in equation (26) yields

$$\Delta S_0 \approx \frac{4\pi R^2 \sin \psi_{0P}}{\eta \cos \psi_{0P}} \tag{28}$$

Finally the acoustic power in the principal lobe can be estimated by,

$$P_p^2 \Delta S_0 \approx \left(\frac{\eta \cos \psi_{0P}}{2 \sin \psi_{0P}} \right) \left(\frac{4\pi R^2 \sin \psi_{0P}}{\eta \cos \psi_{0P}} \right) = 2\pi R^2 \tag{29}$$

Thus, at a constant radius the acoustic power in the principal lobe is constant no matter where it is located. The far-field pressure fall-off toward the side-line is due only to an increase in the incremental far-field area. The R^2 factor remains in equation (29) since it was eliminated in the derivation of the directivity factor presented by equations (1) or (4).

In a manner very similar to the above, the far-field area subtended by the principal lobe of radiation from a duct with jet flow and a surrounding medium separated by a slip layer can be derived. The derivation is far more complicated since the several angular transformations going from ψ_D to φ_D to φ_f to ψ_f must be used. The final result is,

$$\Delta S_f \approx \frac{4\pi R^2 \sqrt{1 - 2M_D \cos \psi_{fP} - \left(1 - M_D^2\right) \cos^2 \psi_{fP}}}{\eta \left[M_D + \left(1 - M_D^2\right) \cos \psi_{fP} \right]} \tag{30}$$

By analogy with equation (29) the principal lobe peak can be estimated by,

$$p_{fP}^2 \approx \frac{2\pi R^2}{\Delta S_f} \approx \frac{\eta\left[M_D + \left(1 - M_D^2\right)\cos \psi_{fP}\right]}{2\sqrt{1 - 2M_D \cos \psi_{fP} - \left(1 - M_D^2\right)\cos^2\psi_{fP}}} \tag{31}$$

As in reference 6 the mutlimodal pressure squared will be estimated by multiplying the principal lobe peak by the number of modes whose principal lobe can contribute at a particular angle. By using the transformations of equations (5) and (6) in equation (4), the cut-off ratio range which can contribute is seen to be from,

$$\frac{1}{\xi_{D1}} \approx \frac{\beta \sin \psi_D}{\sqrt{1 - M_D^2 \sin^2\psi_D}} - \frac{\beta}{\eta} \tag{32}$$

up to

$$\frac{1}{\xi_{D2}} \approx \frac{\beta \sin \psi_D}{\sqrt{1 - M_D^2 \sin^2\psi_D}} + \frac{\beta}{\eta} \tag{33}$$

These can be used in the integration of the modal density function[17] to obtain,

$$N \approx \int_{\xi_{D2}}^{\xi_{D1}} \frac{2}{\xi_D^3}\, d\xi_D \approx \frac{4\beta^2 \sin \psi_D}{\eta\sqrt{1 - M_D^2 \sin^2\psi_D}} \tag{34}$$

This can be transformed to (using equations (10), (14) and (15)),

$$N \approx \frac{4\beta^2}{\eta}\sqrt{1 - 2M_D \cos \psi_{fP} - \left(1 - M_D^2\right)\cos^2\psi_{fP}} \tag{35}$$

The multimodal (equal acoustic power per mode) radiation pattern is then estimated by,

$$p_{fM}^2 \approx p_{fP}^2 N \approx 2\left(1 - M_D^2\right)\left[M_D + \left(1 - M_D^2\right)\cos \psi_f\right] \tag{36}$$

where the general far-field angle ψ_f replaces ψ_{fP}. Note that when $M_D = 0$ equation (36) reduces to $2 \cos \psi_f$, which is the same result as in reference 6. Equation (36) can be used only outside of the zone of silence since both N and $\Delta S_f \to 0$ as $\cos \psi_f \to 1/(1 + M_D)$, and P_{fM}^2 can be seen to peak at this angle. If this value of P_{fM}^2 is used as a normalization, a sound pressure level can be calculated as,

$$SPL_f \approx 10 \text{ Log}\left[M_D + \left(1 - M_D^2\right)\cos \psi_f\right] \tag{37}$$

which can be seen to be a very simple expression for the multimodal, equal acoustic power per mode directivity. This expression will be compared to exact results in the next section.

Exact theory. - The more exact multimodal (equal acoustic power per mode) results were generated using calculations performed on a NASA Langley computer with a Wiener-Hopf radiation program.[13] Only single mode results were available, examples of which have been shown in figures 2 and 3. The condition for the calculations were $M_D = 0.6$ and $\eta = 7.111$. At these conditions, it was estimated there would be 100 propagating modes.[17] The actual count showed that 101 modes could propagate. This provided enough modes to give a fairly smooth radiation pattern while keeping the tedious modal superposition within manageable limits. The approximate equation (37) shows that the radiation pattern for equal acoustic power per mode is a function only of duct Mach number.

Unfortunately, the exact single mode calculations gave no acoustic power number such that they could be readily combined. All results were given with the peak in the radiation pattern having a sound pressure level of 100 decibels. All 101 radiation patterns had to be normalized manually to obtain equal acoustic power per mode. Due to these time consuming procedures only one multimodal example will be shown.

For each single mode radiation pattern the pressure squared term, P_i^2 (arbitrarily normalized) was given at each 5° increment in angle (ψ_f). These values were area weighted to obtain a value which was proportional to the arbitrary acoustic power of the particular mode, using the equation (18),

$$W\left(\frac{\rho c}{4\pi R^2}\right) = \left[\sum_{i=1}^{35} P_i^2 \sin(i\Delta\psi_f)\right] \sin\left(\frac{\Delta\psi_f}{2}\right) \tag{38}$$

where $\Delta\psi_f = 5^\circ$. Each value of P_i^2 was then normalized by the total power using equation (38), thus guaranteeing a particular total acoustic power for the mode. This was repeated for each of the 101 modes. The newly normalized value of P_i^2 for each of these modes was then added over all modes for a given angle (fixed i). This summation of pressure squared terms was then converted into a relative sound pressure level at each angle. The results, representing the combined effects of 101 modes all having equal acoustic power, are shown in figure 4 as the circle symbols. The curve is relatively smooth with the peak occurring just forward of the zone of relative silence. The fall-off toward the inlet axis (180°) is seen to be quite gradual. A large reduction in sound pressure level occurs in the zone of silence just as in the single mode cases.

The approximate radiation pattern for equal acoustic power per mode, equation (37), is also shown in figure 4. The agreement is good over most angles. The exceptions are at the extreme angles, where approximate theory is slightly high at the edge of the zone of silence and quite low toward the inlet axis (large ψ_f). As mentioned previously, the approximate theory could be improved but it is probably good enough for most liner design purposes. Also note that in the zone of silence the approximate theory predicts no radiation while the more exact results show some radiation, although at considerably reduced level as compared to the peak.

Comparison with experimental data. - Noise data for three full scale fans tested statically without inflow control screens will be compared to the multimodal theoretical results. Results for the blade passage tone and the second harmonic will be presented for both take-off and approach speeds. Tables I and II, which were obtained from information in references 19 to 22, present the design and aeroacoustic parameters for the fans designated A, B, and C. The noise data represent narrow band data from which the broadband noise has been subtracted as in reference 23. The theoretical results are from the more exact calculations with equal acoustic power per mode for $M_D = 0.6$ as shown in figure 4. The approximate theory, equation (37), showed about the same calculated results for the Mach number variations encountered here. Thus, the single theoretical curve will suffice for the qualitative comparisons to be made here. It should be noted also that if data compares well with an equal acoustic power per mode radiation theory then a random noise generation process is implied such as might result from blade-turbulence interactions. This appeared to be the case for static fan inlet data as shown in reference 6. The noise data for the blade passage fundamental should be cut-off if caused by rotor stator interaction. The second harmonic has rotor stator interaction modes which can propagate.

The experimental data for the blade passage frequency fundamental at approach speed are compared to theory in figure 5 for the three fans. The data for fans A and C show several similarities with the theory. For angles forward (larger angles) of the zone of silence the slope of the data is quite flat as is the theory. The deviation in the data here may be either scatter or dominant mode peaks. The data also show an abrupt fall-off in the zone of silence. Fan B conversely shows a more gradual fall-off into the zone of silence. No explanation is readily available for this behavior.

In figure 6 for the blade passage frequency at take-off fan speed the theory-data comparison is very similar to figure 5. The higher Mach number, see table II, would cause the zone of silence to move to higher angles. Some hint of this may be seen in the data for fan A. The theoretical calculation has not been adjusted for higher M_D.

The second harmonic noise data at take-off speed are compared to the theory in figure 7. These data are seen to be considerably different from those for the fundamental. Considerable dominant mode lobe patterns are observed for fans A and B. These might be expected since propagating modes are available from the rotor-stator interaction. The considerable penetration of these dominant modes into the zone of silence cannot be explained at this time.

ATTENUATION POTENTIAL FOR INLET AND EXHAUST SUPPRESSORS

During the course of this study of radiation from an exhaust duct, a distinct difference between an inlet and an exhaust duct was observed regarding the relationship between angle of radiation and mode cut-off ratio. The following initial observations are offered although the complete ramifications of the observations have not been investigated. Some additional factors which must be considered are discussed at the end of this section.

To appreciate the following discussion, it must be recalled that the attenuation potential of an acoustic suppressor is dependent upon the modal cut-off ratio or angle of incidence of the sound entering the suppressor. Modes near cut-off (hitting the liner nearly normal) can be attenuated much more easily than modes of high cut-off ratio with mainly axial propagation in the duct. Roughly, the attenuation is inversely proportional to mode cut-off

ratio. Near cut-off modes radiate nearly normal to the engine axis and can therefore have a large impact on fly-over noise, since the distance between the aircraft and the observer are minimized. Nearly axial propagating noise usually travels a long distance and is thus considerably attenuated when it reaches the observer.

The angular location of the peak of the principal lobe of radiation for both inlets (see reference 4, equation (33)) and exhaust ducts (equation (20) this paper) are shown as a function of mode cut-off ratio in figure 8. Notice that for an inlet at 0.4 Mach number the maximum angle of the principal lobe peak is about 66° at cut-off ($\xi_D = 1$). All of the radiation at this angle and larger angles is from near cut-off modes. Thus the direct sideline radiation is quite easily attenuated. For an exhaust duct, however, the radiation at the typical radiation peak of 60° to 70° (see figures 5, 6 and 7) and forward towards the direct sideline is composed of principal lobe radiation associated with quite large mode cut-off ratios. This sound will be attenuated much less by a suppressor. Thus, it appears that aft duct sound may be inherently more difficult to effectively suppress than that emanating from the inlet. Another consideration, on the favorable side, is that typically there is more area and greater duct length-to-height ratio available in an exhaust duct than in an inlet.

It is the author's opinion that there is an additional factor working to give less apparent suppression in the exhaust suppressor. Due to the abrupt nature of the exhaust nozzle and the near normal (to the duct axis) direction of the wave front vector for even moderate cut-off ratios, a strong reflection may occur for modes near cut-off. If this is true, then the duct modes which would be absorbed quite easily by the duct suppressor (near cut-off) never are observed in the far-field. It is thus possible that very small far-field attenuations could be observed even though large in-duct attenuations are observed in the exhaust duct.

CONCLUDING REMARKS

The far-field radiation emanating from the end of an exhaust duct has been studied using both approximate and exact methods. This initial study simulates the radiation of internally generated noise (as from a turbofan) from a circular exhaust duct with a resulting jet which differs in velocity from the surrounding medium across a slip layer. The approximate method starts with the relatively simple single mode flanged duct radiation equation for zero flow. A series of angle transformations adds flow and thus convective effects and also refractive effects across the slip layer. The exact method is an available single mode Wiener-Hopf radiation model for a circular duct. The approximate radiation pattern is a very accurate reproduction of the exact results including the radiation principal lobe shape and location as well as the location of the zeroes in the radiation pattern. An approximate multimodal radiation pattern was also derived which provides a simple expression for radiation with equal acoustic power per mode. This also agrees well with an exact equal acoustic power per mode radiation pattern generated using the Wiener-Hopf solutions. Experimental data of narrow band tone noise from static tests were compared to the multimodal radiation pattern. In most cases, for the blade passage fundamental, the data agree qualitatively with the theory. For the second harmonic it is apparent that some dominant radiation is present from a limited number of modes. Finally, some considerable differences between inlet and exhaust radiation became apparent while working with the approximate radiation

theory. It is pointed out that possibly the exhaust noise in the far-field is inherently more difficult to attenuate than the inlet noise using duct suppressors.

REFERENCES

1. E. J. Rice and L. J. Heidelberg, "Comparison of Inlet Suppressor Data with Approximate Theory Based on Cut-Off Ratio," AIAA Paper No. 80-0100 (January 1980). also NASA TM 81386 (1979).

2. L. J. Heidelberg, E. J. Rice, and L. Homyak, "Experimental Evaluation of a Spinning Mode Acoustic Treatment Design Concept for Aircraft Inlets," NASA TP-1613 (1980).

3. A. V. Saule, "Modal Structure Inferred from Static Far-Field Noise Directivity," AIAA Paper No. 76-574 (July 1976). also NASA TM X-71909 (1976).

4. E. J. Rice, M. F. Heidmann, T. G. Sofrin, "Modal Propagation Angles in a Cylindrical Duct with Flow and Their Relation to Sound Radiation," AIAA Paper No. 79-0183 (January 1979). also NASA TM-79030 (1978).

5. M. F. Heidmann, A. V. Saule, and J. G. McArdle, "Analysis of Radiation Patterns of Interaction Tones Generated by Inlet Rods in the JT15D Engine," AIAA Paper 79-0581 (March 1979). also NASA TM-79074 (1979).

6. E. J. Rice, "Multimodal Far-Field Acoustic Radiation Pattern Using Mode Cutoff Ratio," AIAA J., 16, 906-911 (1978).

7. A. V. Saule and E. J. Rice, "Far-Field Multimodal Acoustic Radiation Directivity," NASA TM-73839 (1977).

8. J. M. Tyler and T. G. Sofrin, "Axial Flow Compressor Noise Studies," SAE Trans., 70, 309-332 (1962).

9. D. L. Lansing, J. A. Drischler, and C. G. Pusey, "Radiation of Sound from an Unflanged Circular Duct with Flow," Acoustical Society 79th. Spring Meeting, Atlantic City, NJ (April 21-24, 1970).

10. G. F. Homicz and J. A. Lordi, "A Note on the Radiative Directivity Patterns of Duct Acoustic Modes," J. Sound Vib., 41, 283-290 (1975).

11. Y. C. Cho, "Sound Radiation from Hyperboloidal Inlet Ducts," AIAA Paper No. 79-0677 (March 1979).

12. W. R. Clark and Y. C. Cho, "An Experimental Study of Sound Radiation from Hyperboloidal Inlet Ducts," NASA TM 80109 (1979).

13. S. D. Savkar and I. H. Edelfelt, "Radiation of Cylindrical Duct Acoustic Modes with Flow Mismatch," Report SRD-75-029, General Electric Co., Schenectady, NY (March 1975). also NASA CR-132613 (1975).

14. S. D. Savkar, "Radiation of Cylindrical Duct Acoustic Modes with Flow Mismatch," J. Sound Vib., 42, 363-386 (1975).

15. S. M. Candel, "Acoustic Radiation from the End of a Two-Dimensional Duct, Effects of Uniform Flow and Duct Lining," J. Sound Vib., 28, 1-13 (1973).

16. P. M. Morse and K. U. Ingard, Theoretical Acoustics (McGraw-Hill, New York, 1968), p. 709.

17. E. J. Rice, "Modal Density Function and Number of Propagation Modes in Ducts," NASA TM X-73539 (1976).

18. F. J. Montegani, "Some Propulsion System Noise Data Handling Conventions and Computer Programs Used at the Lewis Research Center," NASA TM X-3013 (1974).

19. F. J. Montegani, J. W. Schaefer, and E. G. Stakolich, "Noise Generated by Quiet Engine Fans. II: Fan A," NASA TM X-3066 (1974).

20. F. J. Montegani, "Noise Generated by Quiet Engine Fans. I: Fan B," NASA TM X-2528 (1972).

21. F. J. Montegani, J. W. Schaefer, and R. F. Schmiedlin, "Noise Generated by Quiet Engine Fans. III: Fan C," NASA TM X-3360 (1976).

22. W. G. Cornell, "Experimental Quiet Engine Program - Summary Report," NASA CR-2519 (1975).

23. A. V. Saule, "Some Observations about the Components of Transonic Fan Noise from Narrow-Band Spectral Analysis," NASA TN D-7788 (1974).

TABLE I. - DESIGN CHARACTERISTICS OF FANS A, B, AND C

Characteristic	Fan A	Fan B	Fan C
Number of rotor blades	40	26	26
Number of bypass guide vanes	90	60	60
Rotor inlet tip radius, m	0.9315	0.9315	0.8675
Outside radius of nominal bypass nozzle,[a] m	0.827	0.827	0.797
Inside radius of nominal bypass nozzle,[a] m	0.556	0.556	0.562

[a]After trimming.

TABLE II. - AERO-ACOUSTIC CHARACTERISTICS OF FANS A, B, AND C

Characeristic	Fan A		Fan B		Fan C	
	Takeoff	Approach	Takeoff	Approach	Takeoff	Approach
Fan rotational speed, rpm	3189	2126	3209	2135	4671	3117
Fundamental blade passage frequency, Hz	2126	1417	1390	925	2024	1350
Frequency parameter,[a] η	11.7	7.77	7.61	5.06	10.3	6.88
Bypass flow, kg/s	379.2	252.9	381.3	253.8	372.7	248.6
Bypass exhaust Mach number[a]	0.708	0.472	0.711	0.473	0.797	0.532

[a]c = 340.294 m/s.

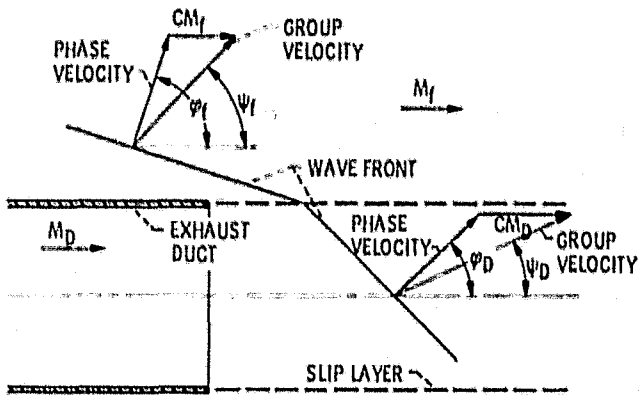

Figure 1. - Angles used in approximate radiation equation.

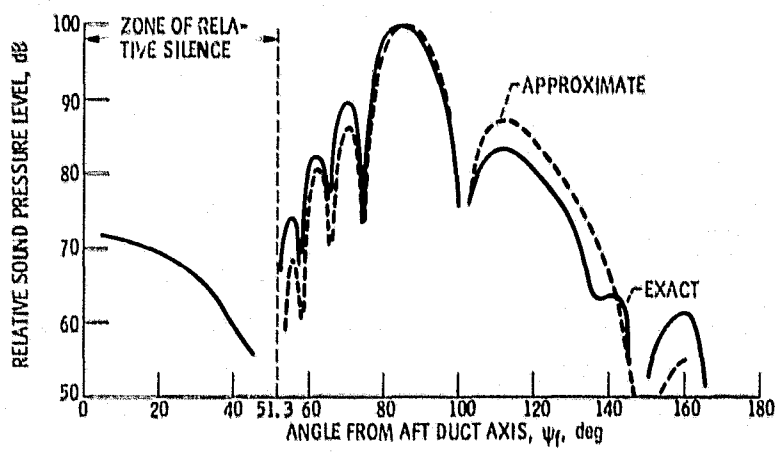

Figure 2. - Comparison of approximate and exact aft radiation patterns for mode (8, 4); $M_D = 0.6$; $M_f = 0$; $\eta = 7.11$.

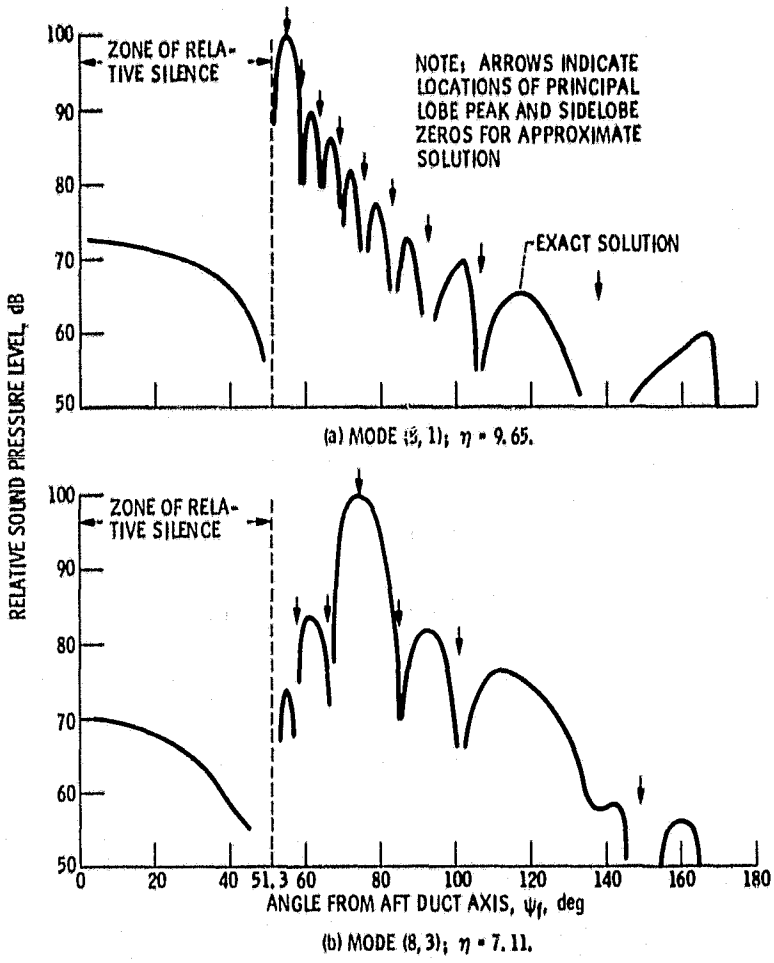

(a) MODE (3, 1); $\eta = 9.65$.

(b) MODE (8, 3); $\eta = 7.11$.

Figure 3. - Comparison of principal lobe peak and sidelobe zero locations of approximate and exact solutions ($M_D = 0.6$; $M_f = 0$).

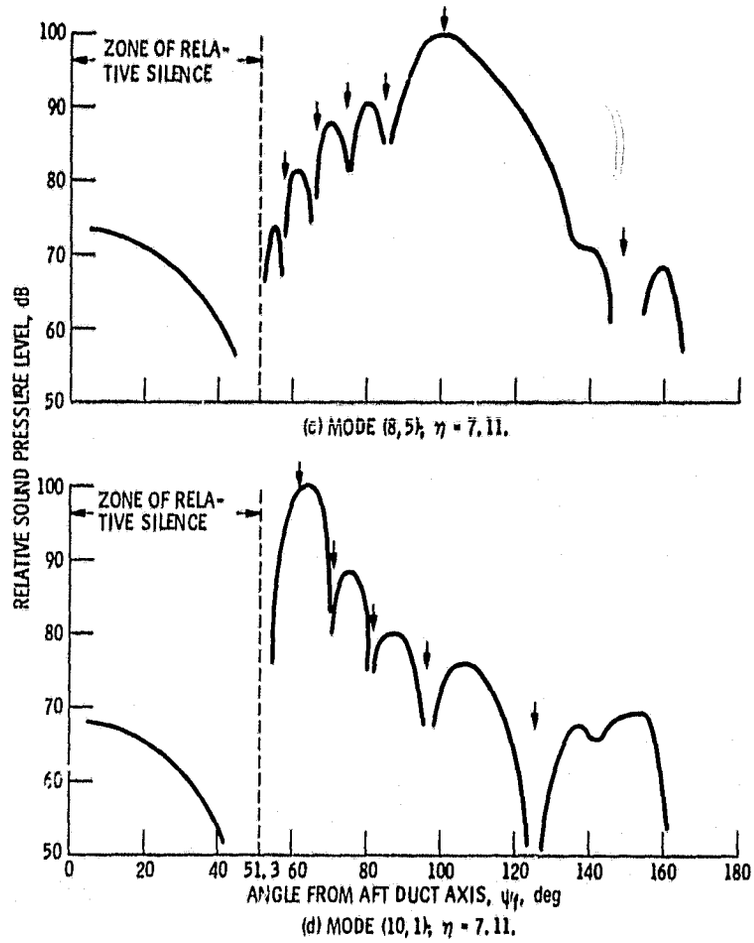

(c) MODE (8, 5); $\eta = 7.11$.

(d) MODE (10, 1); $\eta = 7.11$.

Figure 3. - Concluded.

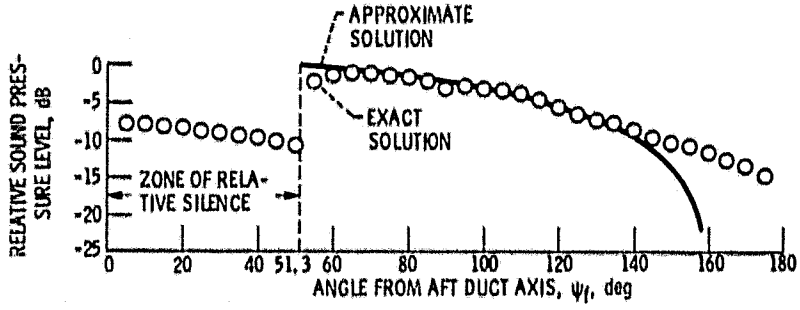

Figure 4. - Comparison of approximate and exact multimodal radiation patterns, 101 modes, equal power per mode, $M_D = 0.6$, $M_f = 0$, $\gamma = 7.11$.

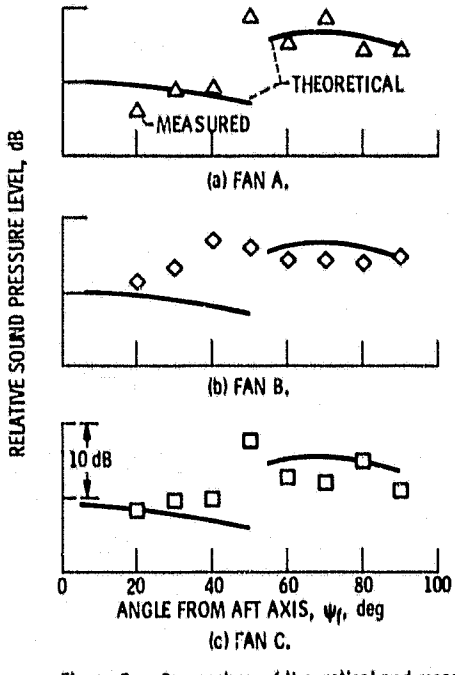

Figure 5. - Comparison of theoretical and measured radiation pattern, blade passage frequency at 60 percent speed.

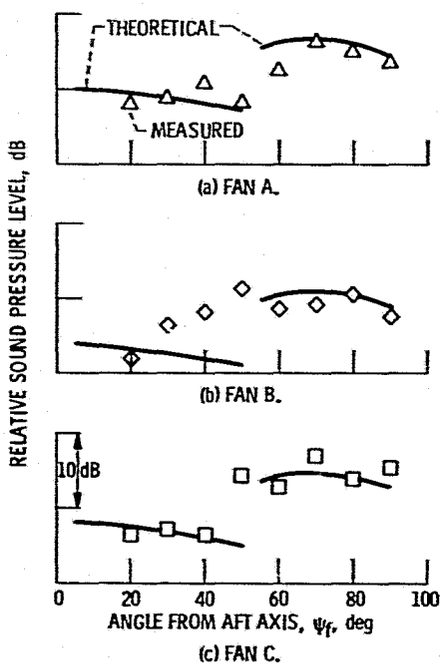

Figure 6. - Comparison of theoretical and measured radiation pattern, blade passing frequency at 90 percent speed.

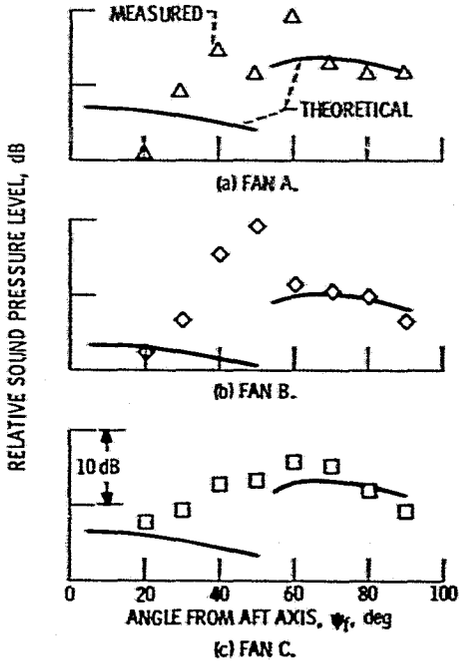

Figure 7. - Comparison of theoretical and measured radiation pattern, second harmonic at 90 percent speed.

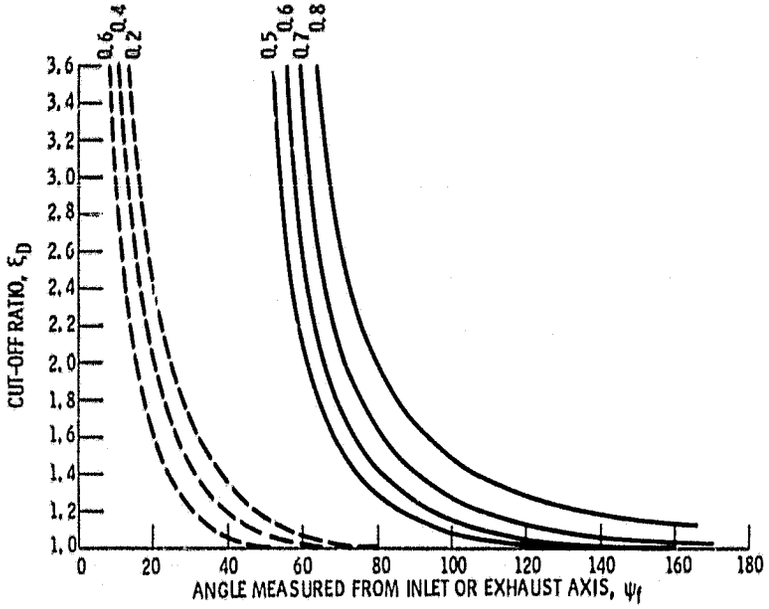

Figure 8. - Location of the peak of principal lobe of radiation as a function of mode cut-off ratio for inlets and aft ducts.